Characteristics of the Near-Surface Currents in the Indian Ocean as Deduced from Satellite-Tracked Surface Drifters. Part I: Pseudo-Eulerian Statistics

SHIQIU PENG AND YU-KUN QIAN

State Key Laboratory of Tropical Oceanography, South China Sea Institute of Oceanology, Chinese Academy of Sciences, Guangzhou, China

RICK LUMPKIN

NOAA/Atlantic Oceanographic and Meteorological Laboratory, Miami, Florida

YAN DU, DONGXIAO WANG, AND PING LI

State Key Laboratory of Tropical Oceanography, South China Sea Institute of Oceanology, Chinese Academy of Sciences, Guangzhou, China

ABSTRACT

Using the 1985–2013 record of near-surface currents from satellite-tracked drifters, the pseudo-Eulerian statistics of the near-surface circulation in the Indian Ocean (IO) are analyzed. It is found that the distributions of the current velocities and mean kinetic energy (MKE) in the IO are extremely inhomogeneous in space and nonstationary in time. The most energetic regions with climatologic mean velocity over $50\,\mathrm{cm\,s^{-1}}$ and MKE over $500\,\mathrm{cm^2\,s^{-2}}$ are found off the eastern coast of Somalia (with maxima of over $100\,\mathrm{cm\,s^{-1}}$ and $1500\,\mathrm{cm^2\,s^{-2}}$) and the equatorial IO, associated with the strong, annually reversing Somalia Current and the twice-a-year eastward equatorial jets. High eddy kinetic energy (EKE) is found in regions of the equatorial IO, western boundary currents, and Agulhas Return Current, with a maximum of over $3000\,\mathrm{cm^2\,s^{-2}}$ off the eastern coast of Somalia. The lowest EKE ($<500\,\mathrm{cm^2\,s^{-2}}$) occurs in the south subtropical gyre between 30° and 40°S and the central-eastern Arabian Sea. Annual and semiannual variability is a significant fraction of the total EKE off the eastern coast of Somalia and in the central-eastern equatorial IO. In general, both the MKE and EKE estimated in the present study are qualitatively in agreement with, but quantitatively larger than, estimates from previous studies. These pseudo-Eulerian MKE and EKE fields, based on the most extensive drifter dataset to date, are the most precise in situ estimates to date and can be used to validate satellite and numerical results.

1. Introduction

The Eulerian and/or Lagrangian statistics of the ocean circulation are important quantities characterizing the physical oceanography features of different ocean basins. Observations by satellite-tracked surface drifters, such as those from the Global Drifter Program (GDP), provide an invaluable tool for investigating the Eulerian or/and Lagrangian statistics of near-surface circulations over different ocean basins, including the Atlantic Ocean (Banyte et al. 2013; Bograd et al. 1999; de Verdiere 1983; Figueroa and Olson 1989; Krauss and Böning 1987; Lumpkin et al. 2002; Rupolo et al. 1996; Rypina et al. 2012; Veneziani et al. 2004; Zhang et al. 2001), Pacific Ocean (Bauer et al. 2002; Bograd et al. 1999; Chaigneau and Pizarro 2005; Lumpkin and Flament 2001; Zhurbas and Oh 2003, 2004), Indian Ocean (Molinari et al. 1990; Shenoi et al. 1999; Zheng et al. 2012), and Southern Ocean (Sallée et al. 2008). Similar studies have been also carried out in some marginal seas, such as the Adriatic Sea (Falco et al. 2000; Maurizi et al. 2004; Poulain 2001; Ursella et al. 2007), Black Sea (Poulain et al. 2005), East Sea (Oh et al. 2000), Mediterranean Sea (De Dominicis et al. 2012),

Corresponding author address: Shiqiu Peng, State Key Laboratory of Tropical Oceanography, South China Sea Institute of Oceanology, Chinese Academy of Sciences, West Xinggang Road No. 164, Guangzhou, China.
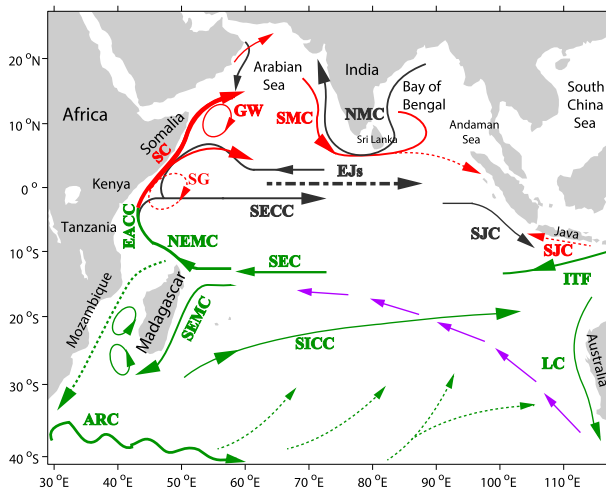E-mail: speng@scsio.ac.cn

FIG. 1. Schematic illustration of the major current systems in the IO, including the South Equatorial Current (SEC), South Equatorial Countercurrent (SECC), South Indian Ocean Countercurrent (SICC), Northeast and Southeast Madagascar Current (NEMC and SEMC), East African Coastal Current (EACC), Somalia Current (SC), Equatorial Jets (EJs, also call Wyrtki jets), Southwest and Northeast Monsoon Currents (SMC and NMC), Northeast and Southeast Madagascar Currents (NEMC and SEMC), South Java Current (SJC), Leeuwin Current (LC), Agulhas Return Current (ARC), Great Whirl (GW), and South Gyre (SG). Currents occurring in summer (winter) are colored red (black), while those occurring in all seasons are colored green. Arrow with black dashed–dotted thick line denotes the EJs occurring during spring and fall. Vectors in magenta denote the subsurface currents. Dashed arrow in the Mozambique Channel shows the effects of eddy propagation. The line thickness here represents the strength of currents roughly.

Norwegian Sea (Andersson et al. 2011; Poulain et al. 1996), South China Sea (Centurioni et al. 2004, 2009; Qian et al. 2013), Tasman Sea (Chiswell et al. 2007), and Tyrrhenian Sea (Rinaldi et al. 2010), as well as in regional current systems, for example, the Algerian Current (Salas et al. 2001) and California Current (Brink et al. 1991; Poulain and Niiler 1989; Swenson and Niiler 1996).

Being the third largest ocean basin of the world and a major part of the largest warm pool on earth, the Indian Ocean (IO) plays an important role in shaping climate on both regional and global scales (Annamalai et al. 2005; Du et al. 2011; Kug and Ham 2012; Schott et al. 2009; Wu and Kirtman 2007; Xie et al. 2009; Zheng et al. 2011). For instance, the Indian Ocean dipole is associated with the variability of the East Asia monsoon and ENSO (Ashok et al. 2004; Luo et al. 2010; Yang et al. 2010). Although the IO circulation systems (see the schematic illustration in Fig. 1) have been given increasing attention by researchers recently, the investigations and studies of the circulation characteristics are still relatively insufficient or less intensive compared to those for other ocean basins, primarily due to the relative

lack of observations in the IO. The earliest studies mapping IO surface currents were mainly based on the compilation of ship drift reports (Defant 1961; Cutler and Swallow 1984), which contain large random errors in the pre-GPS era and biases due to the direct force of the wind on the ships. Satellite-tracked drifting buoys, first deployed in 1975/76 in the western equatorial IO (L. Regier and H. Stommel 1976, unpublished document), provide a much more robust tool in mapping IO surface circulation. Reverdin et al. (1983) and Shetye and Michael (1988) studied the equatorial jets (EJs, also called Wyrtki jets) and the South Equatorial Current (SEC) in the IO, respectively, using measurements from a limited set of drifting buoys. Based on a compilation of 142 surface buoy trajectories deployed during 1975–87 by different organizations, Molinari et al. (1990) mapped the surface current distribution in the tropical IO as well as the seasonal variations of the currents. Shenoi et al. (1999) further explored the near-surface currents and the kinetic energy in the tropical IO by analyzing the trajectories of more (412) satellite-tracked drifting buoys. More recently, Zheng et al. (2012) studied the surface circulations and their seasonal variations in the IO using drifter data from 1979 to 2011 and showed that the basic pattern of the surface circulation in the IO is identical to that revealed by previous studies, although the currents along the eastern coast of Africa appear much stronger. Beal et al. (2013) used two decades of drifter data to describe the seasonal evolution of the surface circulation of the Arabian Sea in the northwestern IO and showed that the drifter data resolved features like the Somalia Current (SC), Great Whirl (GW), and the evolution of monsoon-driven variations that in some respects differ from the well-known schematics of Schott and McCreary (2001) and Schott et al. (2009). Moreover, some studies (e.g., Lumpkin and Johnson 2013; Maximenko et al. 2009; Sudre et al. 2013; Sudre and Morrow 2008) have mapped surface currents over the global ocean, including the IO basin, using all GDP drifter observations available. All of these studies have contributed to reveal the features of surface or near-surface circulation of the IO. These studies, however, have still left much space for a complete and integral investigation of the characteristics of the near-surface circulation across the IO basin. In particular, although a few recent studies have tried to estimate the Lagrangian statistics of the near-surface currents in the IO (Chiswell 2013; Zhurbas et al. 2014), considerable uncertainties of the estimates could exist because of the methods used that may not efficiently remove the impacts of the strong seasonal variability and spatial inhomogeneity of surface currents in the IO (e.g., Qian et al. 2014). Therefore, it is necessary and worthy to carry out a thorough investigation of the Eulerian and Lagrangian

statistics of the near-surface circulation across the IO basin using the most extensive drifter observations ever assembled so far, which motivates the present study. As the first part of this study, this paper focuses on the pseudo-Eulerian statistics (i.e., Lagrangian observations averaged in fixed geographical coordinates) of the near-surface currents, while the Lagrangian statistics will be investigated in a companion paper (Peng et al. 2015, hereinafter PQL2).

In the next section, a description of the methods and the data is given. Section 3 displays the spatial and temporal distribution of the dataset over the IO. The pseudo-Eulerian statistics of near-surface currents are presented in section 4. The final section presents a summary.

2. Data and methods

a. Data

The Lagrangian observations used in the present study are obtained from the National Oceanic and Atmospheric Administration (NOAA) GDP drifter dataset provided by NOAA's Atlantic Oceanographic and Meteorological Laboratory (AOML) (www.aoml.noaa.gov/phod/dac/dacdata.php). AOML's drifter Data Assembly Center assembles the raw data, applies quality control, and interpolates them to uniform 6-h intervals using an optimal procedure known as kriging interpolation (Hansen and Poulain 1996; Lumpkin and Pazos 2007). Velocities are calculated as 12-h centered differences of these positions. This dataset consists of all GDP drifter data with a holey-sock drogue centered at 15-m depth. These drifters follow the near-surface flow in the mixed layer. Until recently, all the drifters were tracked by the Argos satellite system, and the raw fixes of drifter positions are derived from the Doppler shift of their transmission with an accuracy of about 150–1000 m. In the last few years, an increasing number used the Iridium system for data transmission and GPS for location, with accuracy of a few meters.

The present study focuses on the region of the IO (41°S–26°N, 29°–116°E), excluding the South China Sea and Southern Ocean where Eulerian and/or Lagrangian statistics have already been studied recently (e.g., Qian et al. 2013; Sallée et al. 2008). Drifters outside this region are truncated and discarded. No GDP drifter data are available in the IO basin until 1985. Thus, all drifter data from 1985 to the most recent update (June 2013) are chosen for this study, including drogued as well as undrogued drifters that have been recently reanalyzed and updated (Lumpkin et al. 2013).

A drogue is attached to a drifter to reduce the wind-induced slippage and make the drifter move following the mixed layer current. Wind-slip correction is made to drifter velocities for a better representation of the near-surface (mixed layer) currents. For drogued drifters,

NCEP operational 6-h surface winds W (m s^{-1}) are interpolated to the drifter locations and a downwind slip (cm s^{-1}) of $7 \times 10^{-4} W$ is removed from drifter velocities according to Niiler and Paduan (1995). For drifters that have lost their drogues (undrogued drifters), following the practice of Perez et al. (2014), the coefficient for wind-slip correction is obtained by separately calculating time-mean velocities from drogued and from undrogued drifters in all 2° bins with more than 400 6-h observations in the IO region and finding the nondimensional coefficient that, when multiplied by the wind velocity and subtracted from the 6-h undrogued velocities, will minimize the squared differences between drogued and undrogued downwind mean velocities summed over all the well-sampled bins. A coefficient of 1.64×10^{-2} is obtained in this manner to correct undrogued drifter velocities in the IO, which is identical to that of Perez et al. (2014) for the central and eastern equatorial Atlantic, but larger than that (8.6×10^{-3}) of Pazan and Niiler (2001) for the global oceans.

Note that although the correction is designed to minimize the squared difference between drogued and undrogued downwind mean velocity (i.e., first-order moment), it is of interest to see whether it is helpful to reduce the difference of second-order moment such as eddy kinetic energy (EKE). Thus, we compute the EKE from both drogued and undrogued drifters and then show their ratios before and after the wind-slip correction in Fig. 2. Before the correction (Fig. 2a), the EKE of undrogued drifters is larger than that of the drogued over much of the IO (i.e., ratio > 1), especially between 10° and 20°S and the southern part of IO. After the correction (Fig. 2b), these inconsistencies are significantly reduced so that most parts of the IO show near-unity ratios, except the northwest and southeast IO where the numbers of drifter samples are relatively small (Fig. 2). Thus, we believe that the correction has also significantly reduced differences in the EKE (and the diffusivity, another second-order moment) between drogued and undrogued drifters and allows us to incorporate the undrogued data, greatly increasing observational density.

b. Method

Drifter data are first binned into 2° latitude/longitude grids. This grid resolution is chosen as a compromise between sample density within a bin and the resolution of the mean flow. Considering that the currents in the IO may feature strong inhomogeneity in space and seasonal variations in time, the spatial shear and the temporal variability of the flows within a bin should be taken into account to obtain an accurate estimate of the mean and eddy velocities. In this study, drifter observations within a bin are modeled as a series that varies as a function of
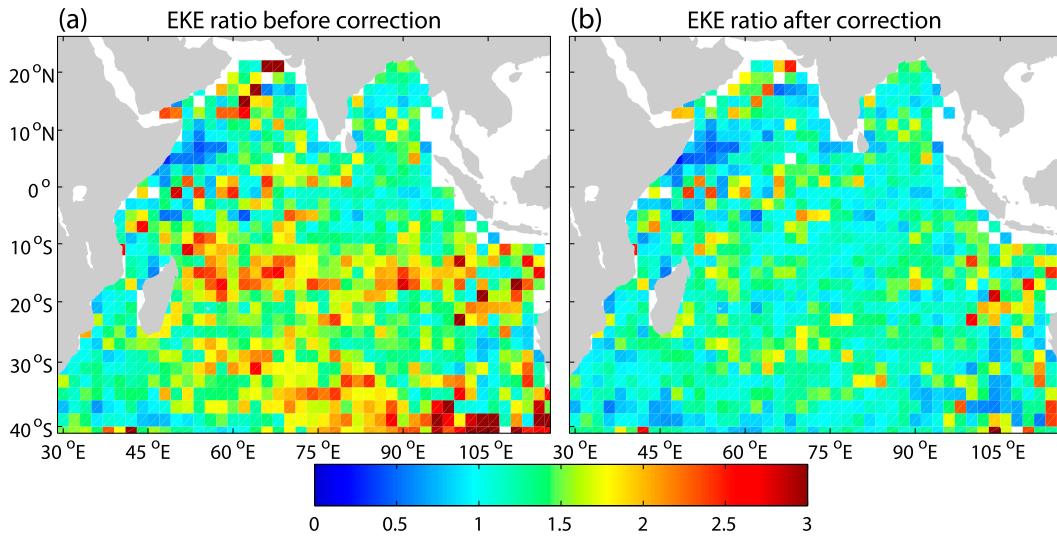
FIG. 2. Ratio of undrogued drifter EKE to drogued drifter EKE (a) before and (b) after wind-slip correction.

both time and space following the method of Lumpkin and Johnson (2013):

$$\mathbf{u} = \mathbf{A}\mathbf{z} + \mathbf{u}', \qquad (1)$$

where the first term stands for a constant mean, the following four terms stand for the annual and semi-annual variability, and the last five terms stand for spatial variability. The terms x_j and y_j are the zonal and meridional distances from a bin center, nondimensionalized by dividing by 1° longitude or latitude. Subscript j indicates that observation j is collected at time t_j (in years). All the components can be fitted to 10 coefficients in $\mathbf{z}$ by adopting the Gauss–Markov (GM) estimator (Lumpkin and Johnson 2013; Wunsch 1996):

$$\mathbf{z} = \mathbf{R}_z \mathbf{A}^{\mathrm{T}} (\mathbf{A}\mathbf{R}_z \mathbf{A}^{\mathrm{T}} + \mathbf{R}_n)^{-1} \mathbf{u}, \qquad (3)$$

where $\mathbf{R}_z$ is the a priori covariance matrix of $\mathbf{z}$, and $\mathbf{R}_n$ is the variance structure of the residual velocity $\mathbf{u}'$. Following Lumpkin and Johnson (2013), each of the diagonal elements of $\mathbf{R}_z$ is assumed to be equal to the squared half range of $\mathbf{u}$, while off-diagonal elements are set to zero and elements of $\mathbf{R}_n$ are chosen as

$$R_n(t) = \mathrm{var}(\mathbf{u}) \cos\left(\frac{\pi t}{2T_d}\right) \exp\left[-\left(\frac{\pi t}{2\sqrt{2}T_d}\right)^2\right], \quad (4)$$

where $\mathbf{u} = (u, v)$ and $\mathbf{u}' = (u', v')$ are original and residual velocity vectors, and $\mathbf{z}$ is the amplitude coefficients for temporal and spatial variability to be determined in matrix $\mathbf{A}$. The components of $\mathbf{A}$ are expressed as

$$A_j = [1 \quad \sin(2\pi t_j) \quad \cos(2\pi t_j) \quad \sin(4\pi t_j) \quad \cos(4\pi t_j) \quad x_j \quad x_j^2 \quad y_j \quad y_j^2 \quad xy_j], \qquad (2)$$

with $T_d = 8.3$ days (equivalent to an integral eddy time scale of 4 days). In (4), $\mathrm{var}(\mathbf{u})$ is the variance of u or v.

3. Distribution of the GDP drifters in the IO

The subset of data collected here spans a total of 1667.7 drifter years with 45.8% drogued and 54.2% undrogued [using the drogue detection method as described by Lumpkin et al. (2013)] after discarding records that are not within the domain (41°S–26°N, 29°–116°E) and those with undefined velocities (endpoints) or those with drifters leaving water (picked up by a ship). Figure 3 displays the number of 6-h drifter observations in 2° bins over the IO. The convergent central-southern IO region has the highest density of drifter observations, up to 9000 6-h samples in a 2° bin. Regions of over 4000 samples include the eastern equatorial IO and east/southeast of Madagascar, and over 2000 samples are found in the central Bay of Bengal (BoB), southeastern Arabian Sea, northwest and south of Madagascar, and west of Australia. The western equatorial IO, south of Java, the Andaman Sea, and the eastern and northern coasts of the Arabian Sea are found to have the sparsest observations with less than 500 6-h samples. Figure 4
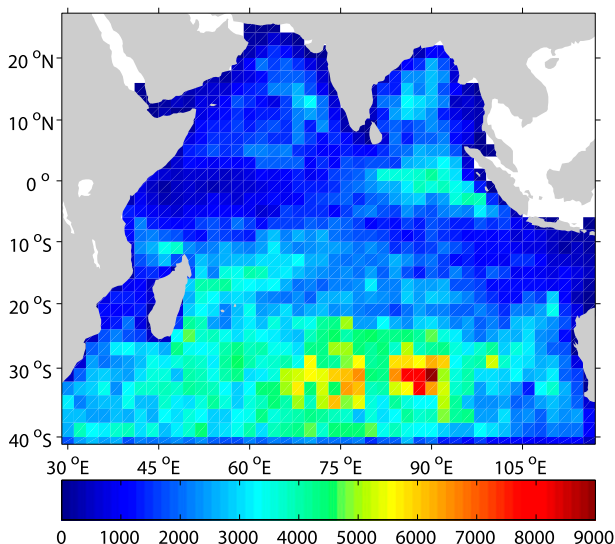
FIG. 3. Number of 6-h GDP drifter observations in 2° bins over the Indian Ocean (41°S–26°N, 29°–116°E) to June 2013.

(2013), we assign each drifter observation a complex number with an amplitude of one unit and a phase of

$$\text{phase} = \frac{\text{day-of-year}}{D} \times 2\pi, \quad D = \begin{cases} 365 & \text{non-leap year} \\ 366 & \text{leap year} \end{cases},$$

where the day of year starts with 1 for 1 January and ends at 365 (366) for 31 December in a nonleap (leap) year. When these numbers are averaged within our 2° bins (Fig. 5), near-zero amplitude indicates homogeneous sampling through all seasons, while near-unity amplitude represents exclusive sampling of one season. Large amplitudes (>0.3) are found primarily in the southern equatorial IO, southwest of Sumatra, and the northern Arabian Sea (where sampling is biased toward April); in the western BoB and south of Java (December–January); and in the Andaman Sea, southeastern BOB, and southeastern Arabian Sea (July–November).

It is of interest to examine the distribution of drifter observations in different speed ranges (Fig. 6). Generally, for both zonal and meridional components, the number of drifter observations appears more like an exponential distribution, especially at large velocity tails (magnitude > 80 cm s^{-1}). The tails of this distribution indicate a higher probability of experiencing anomalously large positive or negative velocities even compared to an exponential. This behavior has been observed in Lagrangian floats over the Atlantic Ocean (e.g., Bracco et al. 2000). Figure 7 gives the spatial distribution of drifter speeds in different ranges. Observations with speeds larger than 100 cm s^{-1} are found in the eastern coast of Africa, equatorial IO, eastern coast of India, eastern–southern coast of Sri Lanka, south-southeast of Madagascar, southeast of the tip of South Africa, and west of Australia, associated with the strong

shows the yearly and monthly variations of the number of drogued and undrogued drifter observations during 1985–2013. Although drifters were present in the IO as early as 1985 (with 270 observations), drifter observations throughout the IO basin were not sustained until 1994 (Lumpkin and Pazos 2007). The total number of drifter observations shows two dramatic increases; one started from 1995 and fluctuated around 100 000 while another started from 2006 and fluctuated around 150 000. The number of observations varied slightly with different months, but the overall observations do not show significant seasonal sampling bias (Fig. 4b).

To display seasonal sampling bias and its spatial distribution, following Lumpkin (2003) and Qian et al.
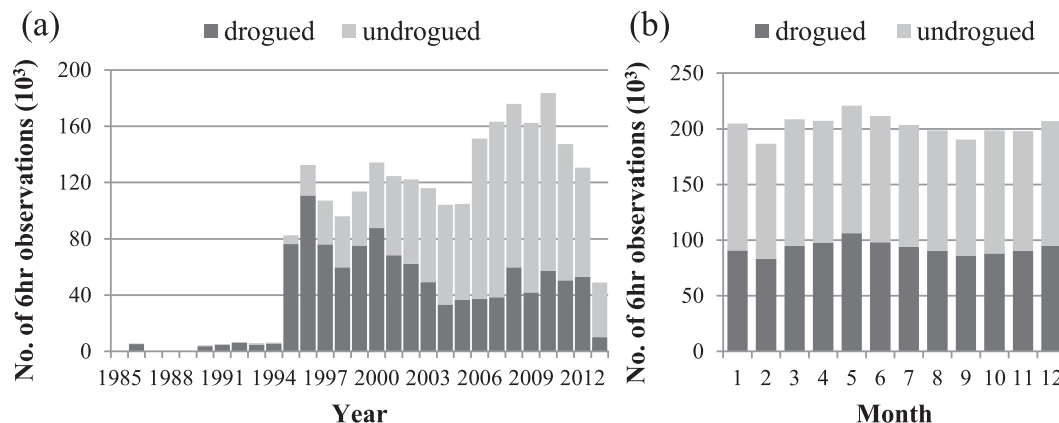

FIG. 4. Temporal distribution of the number of 6-h GDP drifter observations as a function of (a) year and (b) calendar month within the Indian Ocean (41°S–26°N, 29°–116°E). This subset spans the period from 1985 to June 2013, composing 1667.4 drifter year observations.
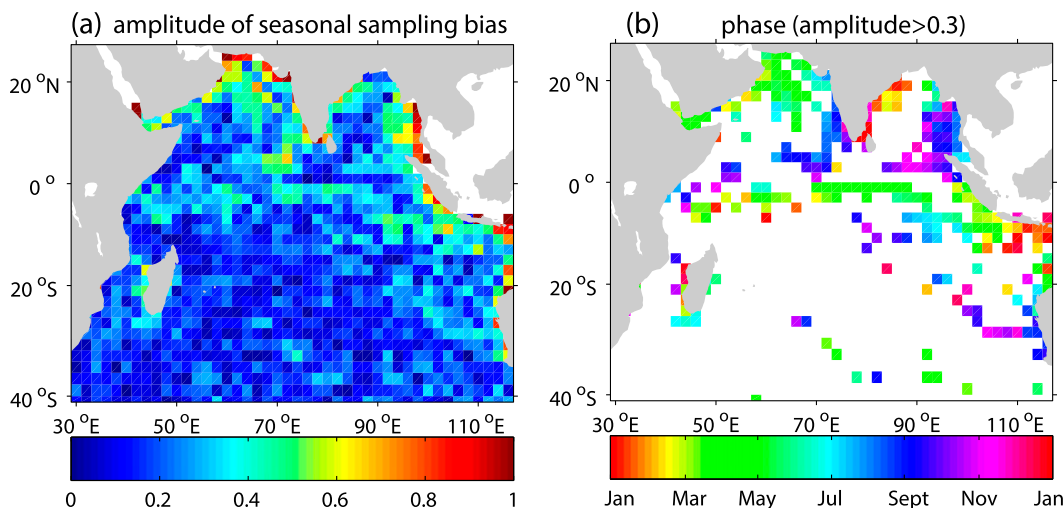
FIG. 5. (a) Amplitude of the seasonal observational bias and (b) the corresponding phase (degree) in 2° bins. Phases are shown where amplitudes are larger than 0.3.

near-surface currents in these regions, while those with speeds larger than 200 cm s^{-1} mainly occur in the eastern coast of Somalia attributed to the strong SC and the offshore currents associated with strong upwelling. The drifter movements in the Mozambique Channel generally show a circular path with large speeds up to 200 cm s^{-1}, confirming the existence of the strong poleward-propagating eddies documented in some studies (e.g., de Ruijter et al. 2002; Schouten et al. 2002, 2003; Swart et al. 2010).

Figure 8a displays some typical drifter trajectories that depict the main currents (see Fig. 1) in the IO basin,

including the SEC (drifters 1–4), the Northeast (drifters 1, 2, and 4) and Southeast (drifter 3) Madagascar Currents (NEMC and SEMC), the South Equatorial Countercurrent (SECC) and EJs (drifter 1), the East African Coastal Current (EACC) and SC (drifter 4), the Southwest Monsoon Current (SMC; drifter 5), the South Java Current (SJC; drifters 1 and 6), the Agulhas Return Current (ARC; drifter 7), and the Leeuwin Current (LC; drifter 8). It is worth noting that drifters at nearly the same location can take quite different paths (1 and 2) and that drifters can travel in opposite directions at different times (7 and 8), indicating the temporal and
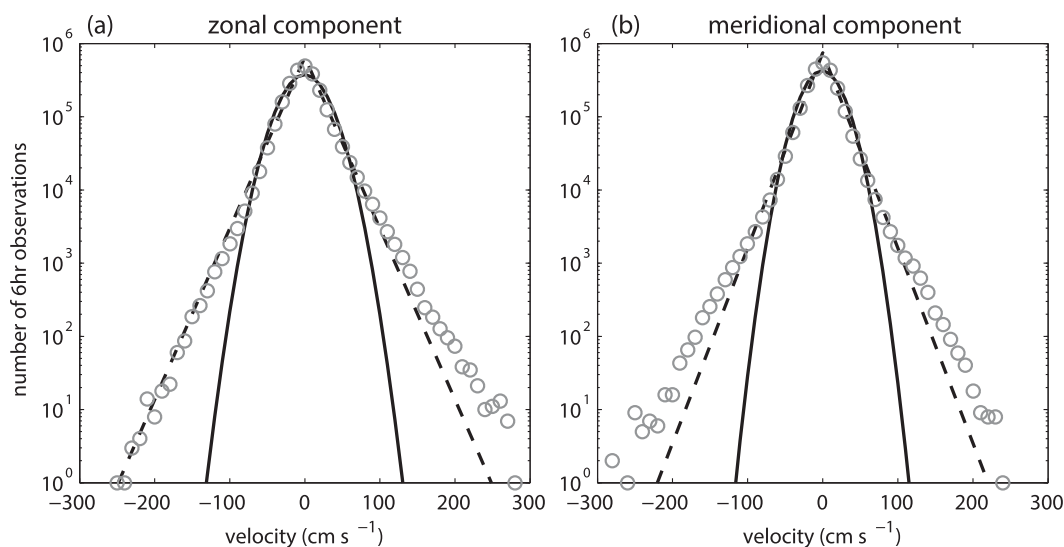

FIG. 6. Drifter-observed (a) zonal and (b) meridional velocity (cm s^{-1}) distribution after wind-slip correction. Black solid and dashed lines are fitted Gaussian and exponential distributions.
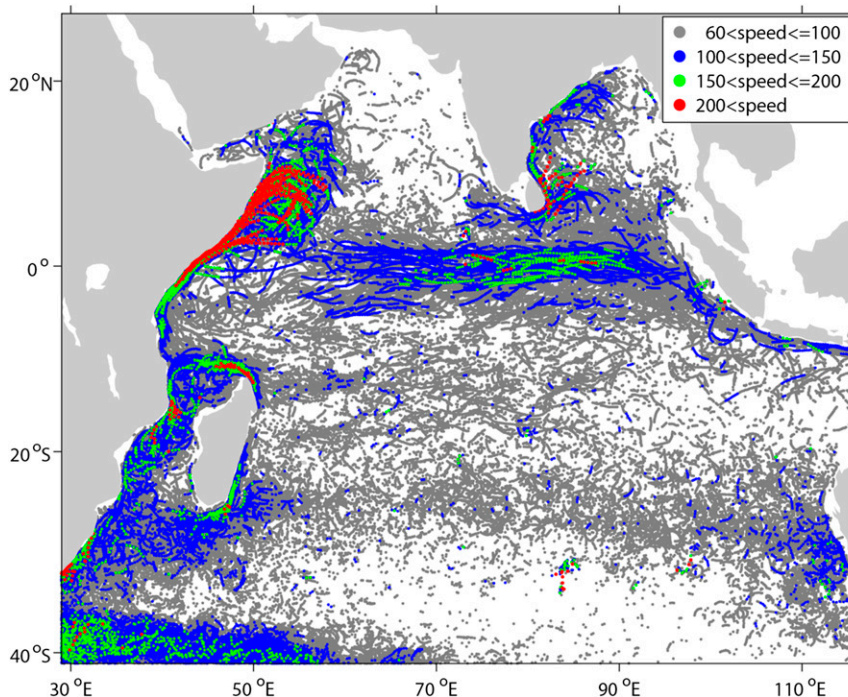
FIG. 7. Distribution of drifter speed larger than $60 \, \text{cm s}^{-1}$.

spatial variability of the circulations in the IO basin. In particular, the SEC bifurcation into the NEMC and SEMC is clearly depicted northeast of Madagascar from drifters 1–4 in Fig. 8a, and swirling behavior is seen for most of the drifters that passed through the Mozambique Channel or traveled southeast of Madagascar after the SEC bifurcation (Fig. 8b), which implies a chain of eddies migrating southward or southwestward around Madagascar (de Ruijter et al. 2004).

4. Pseudo-Eulerian statistics of the near-surface currents

a. Climatologic-mean velocities and kinetic energy

The climatologic-mean velocities of near-surface currents derived from drifters may be influenced by a number of factors, including the selected bin size, the seasonal sampling bias, and so on. The seasonal sampling biases of the drifter observations are inevitable in
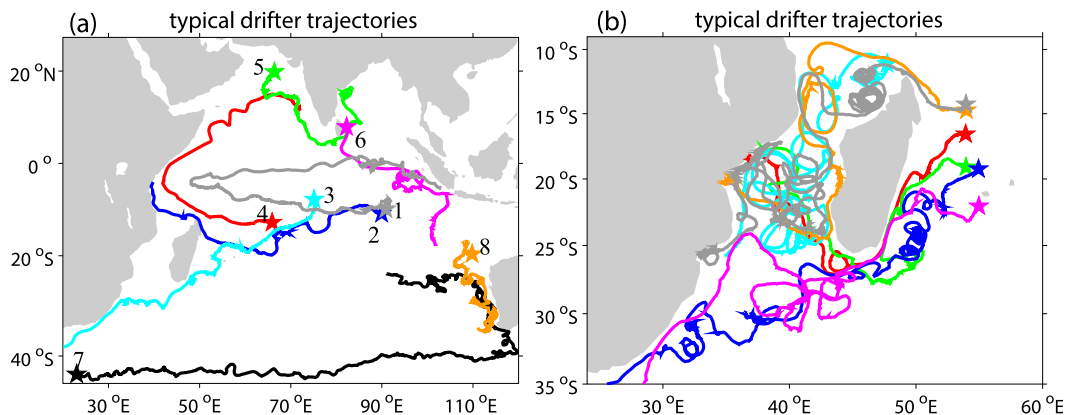

FIG. 8. Typical drifter trajectories over (a) the whole Indian Ocean basin and (b) around the Mozambique Channel. Drifters in (b) are selected when they entered the Mozambique Channel (between 22° and 21°S). The time lengths for the drifter trajectories in (a) are 1) 21 Feb 2009–28 May 2010; 2) 12 Nov 2005–23 Aug 2006; 3) 1 Apr 2011–3 Apr 2012; 4) 15 Apr 2004–9 Oct 2004; 5) 21 Feb 2008–13 Nov 2008; 6) 31 Oct 2001–8 Aug 2002; 7) 21 Feb 2006–30 Nov 2007; and 8) 24 Jan 1998–25 Dec 1998.
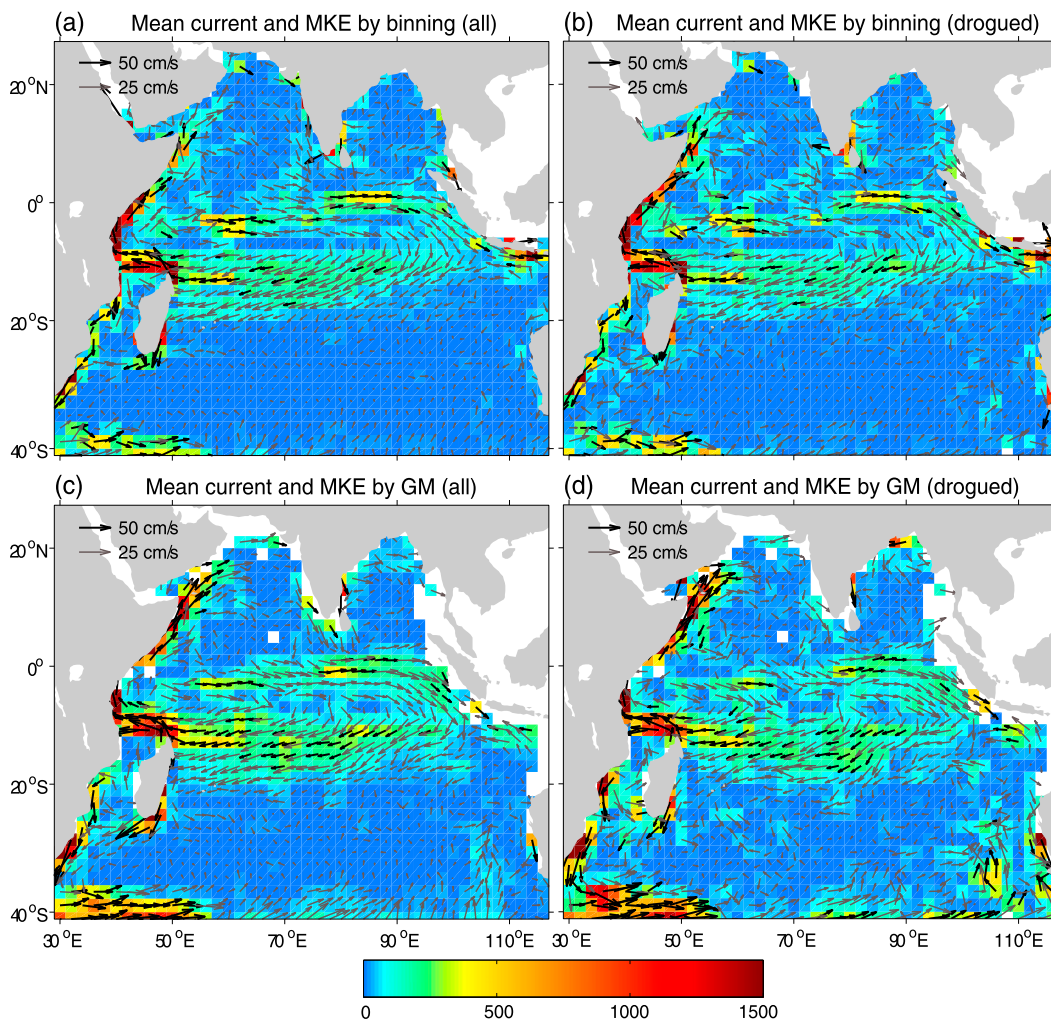
FIG. 9. Eulerian-mean surface current vector ($cm\,s^{-1}$) and mean kinetic energy (shaded, $cm^2\,s^{-2}$) in 2° bins using (a) simple bin averaging and (c) the GM method. (b),(d) As in (a) and (c), but for deriving from drogued-only observations. A 9-point smooth operator is applied to (c) and (d). In (c), bins with <32 6-h observations (roughly two independent observations assuming a 4-day integral time scale) are discarded and the same mask is applied to (d) for comparison.

some regions, as shown in Fig. 5, and intense currents with strong annual/semiannual variability exist in the IO, such as the SC and the EJs. Therefore, the traditional method used to obtain the mean velocities, which averages the drifter-derived velocities within a bin, may introduce considerable biases where observations are mostly within a specific season (e.g., Qian et al. 2013). The GM decomposition method described in section 2, fitting the temporal variability in a continuous harmonic sense, is efficient in reducing such bias induced by the simple binning method. In addition, the GM method can take into account lateral velocity shear (spatial variation) within a bin (Lumpkin and Johnson 2013) and thus can reproduce more realistically the mean currents with strong shear that could be overly smoothed by the

binning method. Therefore, we employ the GM method to obtain the climatologic-mean velocities and kinetic energy.

To see the difference between the two methods, Figs. 9a and 9c display the mean currents and the corresponding mean kinetic energy obtained by the simple binning method and the GM method. The mean currents obtained from both methods capture the major features of the near-surface circulation in the IO basin revealed by ship drift reports or satellite-tracked drifter data or satellite imagery from different data archives, as reported in a number of studies (e.g., Cutler and Swallow 1984; Molinari et al. 1990; Schott and McCreary 2001; Schott et al. 2009; Shenoi et al. 1999; Shetye and Gouveia 1998; Shetye and Michael 1988): the clockwise

rotating South Tropical Gyre (STG) and the anticlockwise rotating South Subtropical Gyre (SSG) in the southern IO; the broad westward SEC between 8°S and 20°S, the narrow eastward SECC south of western equatorial IO between 0° and 5°S, and the eastward EJs in the central-eastern equatorial IO, which generally have mean speed values of 30–50 cm s^{-1} and act as the southern and northern boundaries of the STG, respectively; and the northward (southward) western boundary currents along the eastern coasts of Tanzania, Kenya, and Somalia (Mozambique and South Africa) with mean speed values of over 50 cm s^{-1}. Significant differences are seen in a careful comparison between the two methods: the mean velocities from the GM method are stronger in the regions of the SC, SEC, the eastern coast of South Africa, and the ARC, as compared to those from the simple binning method. Since obvious seasonal sampling biases are not found in these regions (Fig. 5), these differences are attributed to the strong shear (gradient) of the mean flows that could be overly smoothed by the simple binning method. Moderate differences are found east of India, north of the BoB, south of Java, and west of Australia. These differences seem to be caused not only by spatial gradients near the coasts, but also by obvious seasonal sampling biases (Fig. 5); however, as the number of observations in these regions is small (Fig. 2), it is hard to say which one is dominating. The maximum mean speed from the GM method reaches 80 cm s^{-1} in the eastern coast of Somalia and northwest of the northern tip of Madagascar, associated with the SC and NEMC. Obviously, the simple binning method oversmooths the currents in regions where strong spatial variation occurs.

Mean currents derived from only drogued observations are also presented in Figs. 10b and 10d to show the effects of wind-slip correction for undrogued drifters. For the binning method, the drogue-only (Fig. 9b) and all drifter (Fig. 9a) observations result in quite similar results. This is because the wind-slip correction coefficient is obtained through minimizing the differences of bin mean currents between drogued and undrogued drifters. For the GM method, the drogue-only mean currents (Fig. 9d) are not as smooth as those derived from all drifters, especially south of 10°S. More than half of the total observations in this region are undrogued drifter observations (figure not shown). Therefore, significant reduction of the data samples may introduce large errors in the GM decomposition since the GM method depends not only on sample means, but also on sample variances. Another important factor that accounts for such differences is that drogued and undrogued observations sample the currents at difference times and positions. Thus, exactly the same results cannot be expected. It is still

worth noting that wind-slip behaviors depend on drifter types, ocean regions, and wind speed range; thus, a single correction coefficient may not reflect various situations. A single coefficient is adopted here for simplicity, for reducing the systematic bias in the first-order moment (e.g., Eulerian-mean current), and most importantly for incorporating another half of the drifter observations losing their drogues. As already shown in Fig. 2, biases of the second-order moment (e.g., EKE) are also reduced by such a single coefficient.

The mean kinetic energy (MKE) shown in Fig. 9 is defined as

$$\mathrm{MKE} = \frac{1}{2}(\langle u \rangle_E^2 + \langle v \rangle_E^2), \qquad (5)$$

where $\langle\ \rangle_E$ denotes the Eulerian ensemble average within 2° bins. High values of MKE occur in the equatorial IO, eastern coast of Africa, and the southwestern edge of the IO with a maximum of ~1500 cm^2 s^{-2}, whereas low values are present in the south subtropical IO, central Arabian Sea, and central BoB. The distribution of MKE in the IO presented here qualitatively agrees with that obtained by Wyrtki et al. (1976) using ship drift and by Shenoi et al. (1999) using drifters. There are, however, large quantitative differences between the present study and the previous ones. The values of MKE obtained in this study are much larger. For example, the values of MKE in the equatorial region and SEC region are in the range of 300–500 cm^2 s^{-2} in this study compared to 50–100 cm^2 s^{-2} in Wyrtki et al. (1976) or 100–200 cm^2 s^{-2} in Shenoi et al. (1999). Similarly, off the eastern coast of Africa, the values of MKE reach 1500 cm^2 s^{-2}, whereas those in Shenoi et al. (1999) are about 1000 cm^2 s^{-2} and those in Wyrtki et al. (1976) do not exceed 500 cm^2 s^{-2}. The coarse spatial resolution of 5° grids in Wyrtki et al. (1976) and the errors inherent in the ship drift measurements are believed to be the main reasons causing the low MKE in that study (Patterson 1985; Shenoi et al. 1999). On the other hand, as admitted by Shenoi et al. (1999), although the dataset used in Shenoi et al. (1999) was the most extensive one by that time (up to August 1998), estimates of MKE were still subject to large uncertainties because of the largely inhomogeneous and relatively sparse distribution of drifters and because of the limits inherent in simple bin averaging. Therefore, with the most extensive drifter data ever assembled to date (up to June 2013), the estimates presented here are believed to be a more precise update of those in previous studies.

b. Temporal variability and eddy kinetic energy

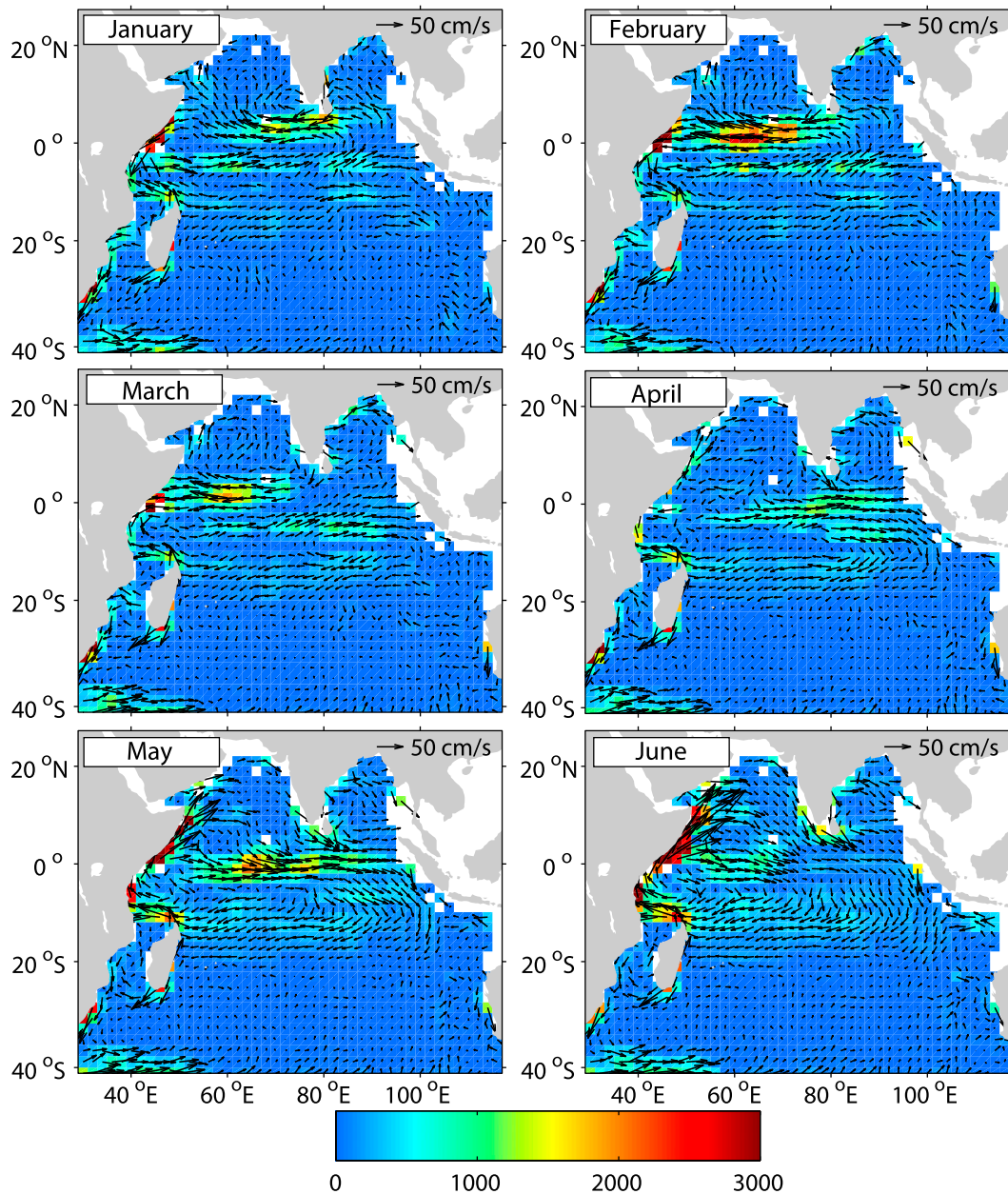Figure 10 shows the monthly-mean near-surface currents and MKE reconstructed by the GM method. The

FIG. 10. Monthly-mean surface current vectors ($cm\,s^{-1}$) and mean kinetic energy (shaded; $cm^2\,s^{-2}$) derived from GDP drifters. A 9-point smooth operator is applied to each month.

apparent seasonal variations of the near-surface circulation can be clearly seen in the SC, EJs, and Northeast Monsoon Current (NMC)/SMC, which are associated with the annually reversing monsoons and are generally in agreement with those of Shenoi et al. (1999), Molinari et al. (1990), and Beal et al. (2013). The northeastward SC begins to develop in April with the onset of the southwest monsoon, peaks in July with a maximum of monthly-mean speeds (hereinafter speeds) $> 150\,cm\,s^{-1}$, and lasts until October when the southwest monsoon

starts to diminish; it reverses its direction and flows southward in December with the onset of the northeast monsoon, reaches its maximum in January with a maximum of speeds $> 100\,cm\,s^{-1}$, and weakens in March. The EJs develop during the transitions between the monsoons, that is, during April–May and October–December, and peak in November with maximum speeds $> 100\,cm\,s^{-1}$. The westward/northwestward NMC develops south/southwest of India to the east of Somalia in December, reaching its maximum of 50–60 $cm\,s^{-1}$ in February with
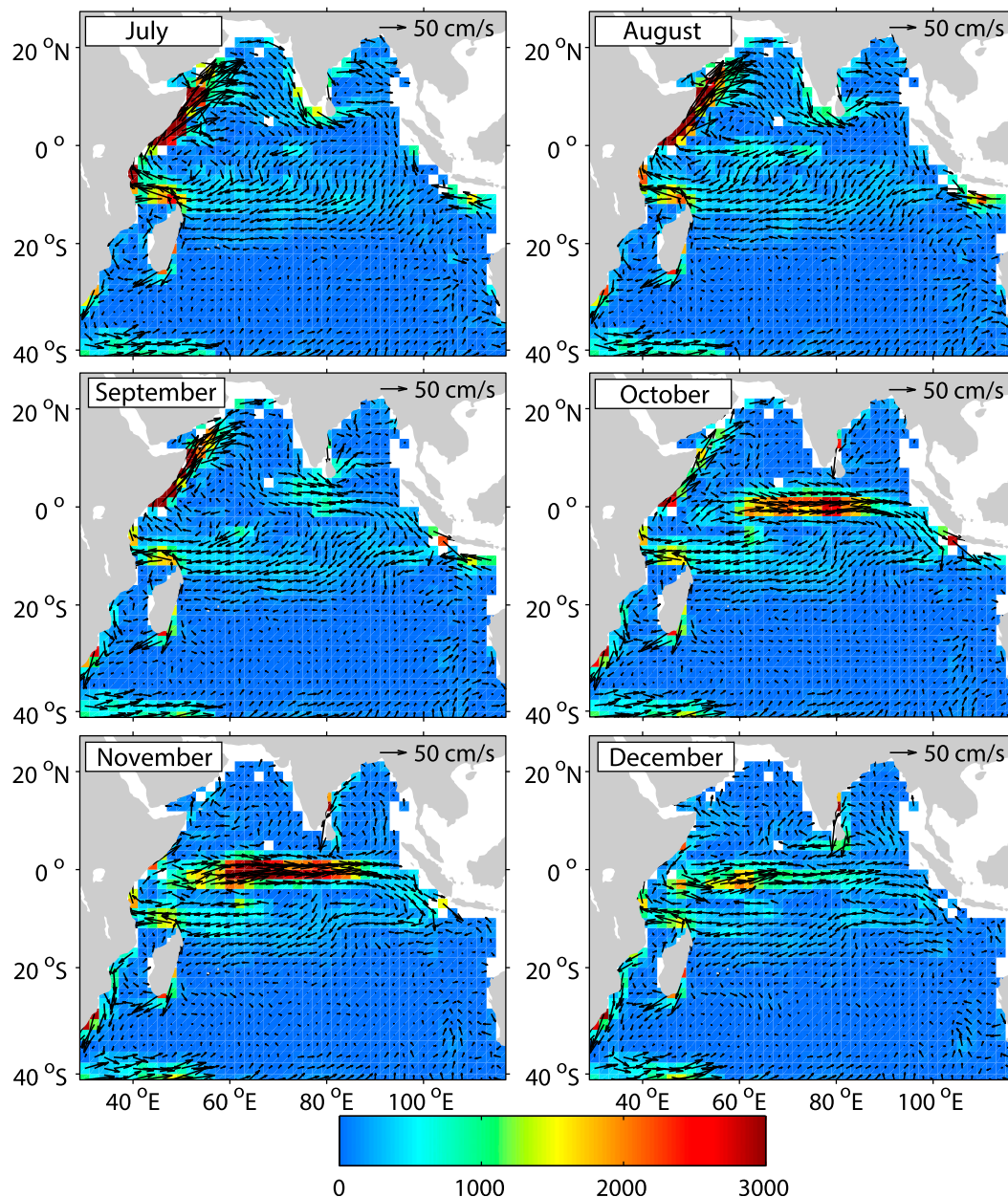
FIG. 10. (*Continued*)

its axis near the equator, whereas Shenoi et al. (1999) reported a maximum of 30–40 cm s^{-1} in February with its axis around 5°N. Beginning in April, the westward/ northwestward NMC begins to be replaced by the eastward/southeastward SMC that emerges first south of India and then extends to southwest/west of India and the northern Arabian Sea, reaching its maximum in July and fading away in October. Similar to Shenoi et al. (1999), a clockwise gyre is seen in the BoB during January–April, while an anticlockwise gyre occurs

during October–December. It is worth noting that a narrow westward flow south of the equator between 50° and 80°E occurs in August, which is in agreement with the satellite drifter-based analysis of Shenoi et al. (1999) and the model-simulated results of McCreary et al. (1993), but not indicated in the ship drift–based analysis of Cutler and Swallow (1984). As to the distribution of monthly-mean kinetic energy, the most energetic regions are found along the eastern coast of Africa during May–September and over the equatorial
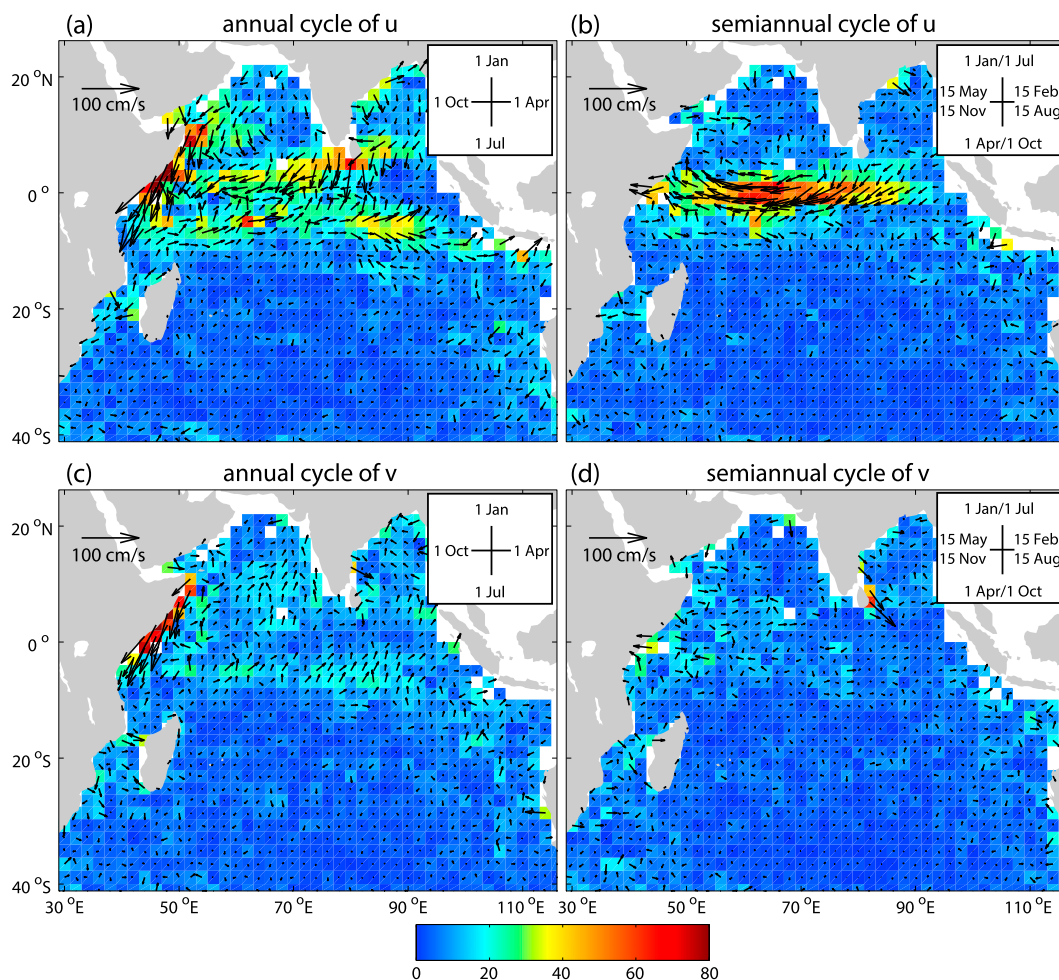
FIG. 11. Amplitude (vector length and shaded; cm s^{-1}) and phase (vector angle) of the (a),(c) annual and (b),(d) semiannual cycles for (left) zonal and (right) meridional surface currents, derived by the GM method. Bins with <32 6-h observations (roughly two independent observations assuming a 4-day integral time scale) are discarded.

IO during February–May and October–December, with a maximum value $> 10\,000\,\text{cm}^2\,\text{s}^{-2}$ that is much larger than that of the climatologic MKE shown in Fig. 9.

The amplitudes and phases of annual and semiannual cycles derived from the GM decomposition are shown in Fig. 11. Annual variability with an amplitude $> 30\,\text{cm s}^{-1}$ is found in the areas associated with the SC, SMC/NMC, SEC/SECC, and SJC that are driven or influenced by the annually reversing Indian monsoon, with the zonal component dominating. Semiannual variability with an amplitude $> 30\,\text{cm s}^{-1}$ is found only in zonal velocities in the equatorial IO corresponding to the twice-yearly EJs driven by the semiannual westerly component during both intermonsoon seasons (Schott et al. 2009). The amplitude of annual variability reaches a maximum of $80\,\text{cm s}^{-1}$ in July east of Somalia for both zonal and meridional velocities (e.g., Beal et al. 2013), while that of semiannual variability shows a maximum of $65\,\text{cm s}^{-1}$

only in zonal velocities, first occurring in the eastern equatorial IO in late April and October and then propagating westward to the central/western equatorial IO in early May and November. This annual and semiannual variability is qualitatively in agreement with, but quantitatively larger than, those presented by Molinari et al. (1990) and Shenoi et al. (1999) that are below $50\,\text{cm s}^{-1}$. It is worth noting that although the SEC is permanently flowing eastward, it intensifies in the boreal summer with its northern edge extending to 5°S and weakens in boreal winter with its northern edge retreating to 10°S (Fig. 10), which could be one of the reasons why an annual variability exists over the region of 5°–10°S. Another explanation is that the seasonal cycle in the Southern Hemisphere trade winds generates an annual Rossby wave in the ocean that manifests as an annual cycle in the SEC (Woodberry et al. 1989; Shenoi et al. 1999).
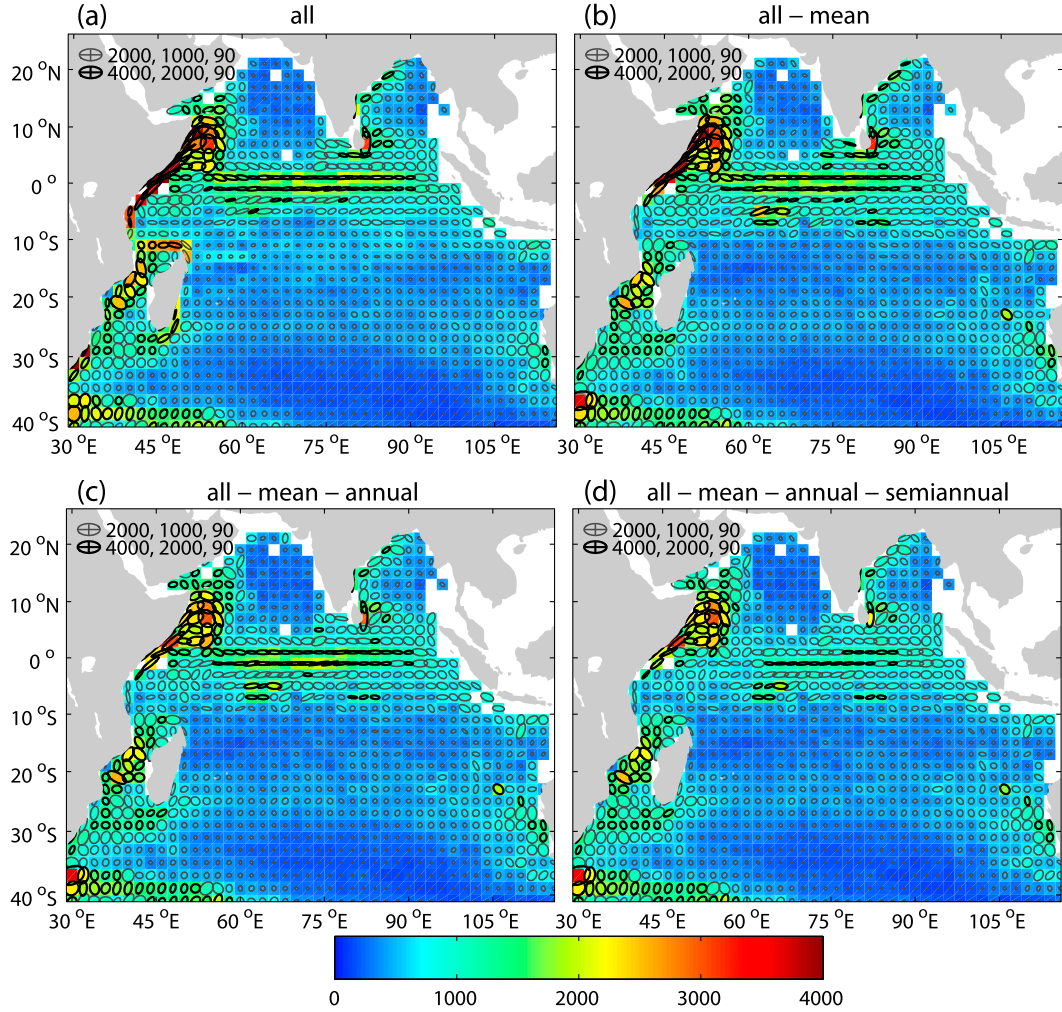
FIG. 12. Kinetic energy (shaded; cm^2 s^{-2}) and variance ellipses computed using drifter-observed surface velocities of (a) all, (b) excluding GM mean, (c) excluding GM mean and annual cycle, and (d) excluding GM mean, annual, and semiannual components. Bins with <32 6-h observations (roughly two independent observations assuming a 4-day integral time scale) are discarded.

To verify the importance of seasonal variability, we have also computed the contribution of each component in the GM model to the total variance, including annual and semiannual cycles, spatial variations, and residuals (figure not shown). Consistent with the amplitude (Fig. 11), the variance contribution of seasonal variability for the zonal velocity can reach a percentage as large as 60%–70% located in the northern-central tropical IO for the annual cycle and the western equatorial IO for the semiannual cycle. Higher percentages (30%–50%) explained by spatial variance are found in the northern Arabian Sea, north of Madagascar, in the southern tropical IO, and west of Australia, indicating the relative importance of mean shear over these regions. The variance explained by the residuals is >80% in the central-western BoB, eastern tropical IO, and the whole southern IO.

Figure 12 shows the total kinetic energy (TKE) and EKE as well as the corresponding variance ellipses, which are calculated from the drifter-observed total (including mean) velocities and residual velocities as follows:

$$\text{TKE} = \frac{1}{2}\langle u^2 + v^2 \rangle_E, \tag{6}$$

$$\text{EKE} = \frac{1}{2}\langle u'^2 + v'^2 \rangle_E, \tag{7}$$

where $\langle\ \rangle_E$ denotes the Eulerian ensemble average within each 2° bin, and the residual velocity components u' and v' are calculated by subtracting the mean, annual, and semiannual components (via the GM decomposition). Note that the residual velocity in the EKE calculation are

defined as the departure from a mean plus seasonal cycles, instead of the departure from a constant mean as adopted traditionally, to show the influence of the seasonal cycles on the EKE as well as the anisotropy of variance ellipses. Besides, it is convenient to compare these variance ellipses to the diffusivity ellipses shown in PQL2.

For the drifter-derived total velocities, large TKE is in accordance with the strong currents (e.g., SC, EJs, and ARC in Fig. 12a). The distributions of EKE and velocity variance generally follow those of TKE with comparable magnitudes. The impacts of the annual and semiannual variability on EKE and the velocity variances are clearly seen in Figs. 12c and 12d. After excluding the annual and semiannual variabilities (Fig. 12d), large EKE ($>2000\,\mathrm{cm}^2\,\mathrm{s}^{-2}$, corresponding to a root-mean-square speed of over $45\,\mathrm{cm}\,\mathrm{s}^{-1}$) is seen off the eastern coast of Somalia, in the Mozambique Channel, and in the southwestern edge of the IO, indicating intensive eddy activity in these regions with energy comparable to that of mean currents. Besides, eddy energetic regions are also found in the central/eastern equatorial IO, the southern and western rim of the BoB, south of Madagascar, and west of Australia. The lowest values of EKE in the central-eastern Arabian Sea, southern tropical IO between $10°$ and $20°$S, and in the south subtropical IO between $30°$ and $40°$S, where the SSG is located, imply much weaker eddy activity over these regions. Large total velocity variances with significant anisotropy are seen in the regions of the energetic currents (Fig. 12a). Generally, the orientations of the variance ellipses in these variance anisotropy regions follow the directions of mean currents, such as the SC and EJs. When excluding the mean, annual, and semiannual components one by one (Figs. 12b–d), the anisotropy over these regions is reduced significantly over the regions of SC and EJs. However, after excluding the seasonal variability (Fig. 12d), strong anisotropy still exists, indicating that eddies may also induce anisotropy over the SC and EJs. Note that the variance ellipses along the ARC are oriented perpendicular to the ARC, indicating stronger cross-stream than along-stream variation. This is in accordance with Rypina et al. (2012), who found a similar result in the Gulf Stream extension. It is also interesting to notice that obvious anisotropy of velocity variance appears in the middle of the Mozambique Channel, but the orientation of the variance ellipses are mostly northwest–southeast instead of north–south, indicating to some extent once again that the flow is generally composed of southward-migrating eddies (de Ruijter et al. 2002; Schouten et al. 2003; Schott et al. 2009; Swart et al. 2010).

A comparison between the EKE estimated here and that estimated by Shenoi et al. (1999) shows that they agree with each other qualitatively in most regions of the IO, but not quantitatively, and even contradict in some regions. Both show highest EKE in the western boundary and equatorial currents and lowest EKE in the Arabian Sea and BoB. The magnitudes of EKE over these regions, however, are quite different. Since the estimated EKE in Shenoi et al. (1999) includes seasonal variability, it can only be compared with that in Fig. 12b that also includes the seasonal variability. A maximum of $\sim$1600 $\mathrm{cm}^2\,\mathrm{s}^{-2}$ in regions of the west boundary and equatorial currents estimated in Shenoi et al. (1999) is much smaller than that of $\sim$7000 $\mathrm{cm}^2\,\mathrm{s}^{-2}$ shown in Fig. 12b. This study finds an intermediate EKE ridge ($\sim$500–1000 $\mathrm{cm}^2\,\mathrm{s}^{-2}$) between $20°$ and $30°$S and higher EKE ($\sim$1500–2000 $\mathrm{cm}^2\,\mathrm{s}^{-2}$) southeast of the tip of South Africa (i.e., the southwestern flank of the IO), indicating moderate and intensive eddy activity over these regions associated with the South Indian Ocean Countercurrent (SICC) and ARC, respectively, which is not available in the estimate of Shenoi et al. (1999) that only covers regions north of $20°$S. Again, given the most extensive drifter dataset ever assembled to date, the distribution of EKE estimated here is a revised update from previous studies with less uncertainties and consideration of the impacts of the intense seasonal variations.

5. Summary

The Eulerian statistics of the near-surface circulation in the IO basin ($41°$S–$26°$N, $29°$–$116°$E) are investigated based on the long-term (1985–June 2013) record of observations from the GDP satellite-tracked drifters. The distributions of all drifter data are quite inhomogeneous in space and nonstationary in time. The drifter velocities are also spaciously inhomogeneous and statistically display an exponential behavior at high speeds ($>80\,\mathrm{cm}\,\mathrm{s}^{-1}$), indicating a higher probability of experiencing anomalously large positive or negative velocities compared to a Gaussian distribution. High speeds are observed in the equatorial IO and the eastern coast of Somalia, associated with the strong equatorial jets and Somalia Current. In particular, observations of speeds larger than $200\,\mathrm{cm}\,\mathrm{s}^{-1}$ are found radiating northeastward from the eastern coast of Sri Lanka, implying a much stronger offshore current east of Sri Lanka associated with the southwest Indian monsoon than previously ever documented. In contrast, regions with drifter speeds always less than $60\,\mathrm{cm}\,\mathrm{s}^{-1}$ are found in the south subtropical IO, central-northeastern Arabian Sea, eastern BoB, and south of the eastern tropical IO (between $12°$ and $20°$S). The pseudo-Eulerian mean near-surface currents in the IO derived from the GDP drifter observations using the Gauss–Markov decomposition method or the simple binning method are

generally in agreement with those revealed by ship drift reports or satellite-tracked drifters or satellite imagery from other data archives. However, the GM decomposition method is found to reproduce more realistically the mean currents of the IO because it takes into account the lateral velocity shear as well as seasonal sampling bias, whereas the traditionally simple binning method does not. Particularly, the GM method derives stronger mean velocities in the regions with strong velocity shear (such as the SC, SEC, and the ARC) as compared to the simple binning method that tends to oversmooth the mean velocities in these regions.

High climatologic MKE (e.g., $>300 \, \mathrm{cm}^2 \, \mathrm{s}^{-2}$) derived from the GM method is found in regions of western boundary currents and equatorial jets as well as ARC with a maximum of $1500 \, \mathrm{cm}^2 \, \mathrm{s}^{-2}$, whereas low MKE is observed in the south subtropical IO, central Arabian Sea, and central BoB. After excluding the mean, annual, and semiannual cycles, the most eddy energetic regions with EKE $> 2000 \, \mathrm{cm}^2 \, \mathrm{s}^{-2}$ are found in the eastern coast of Somalia, the Mozambique Channel, and the southwestern edge of the IO, indicating intensive eddy activity in these regions with energy comparable to that of mean currents. Eddy energetic regions are also found in the central/eastern equatorial IO, the southern and western rim of the BoB, south of Madagascar, and west of Australia. The lowest values of EKE occur in the central-eastern Arabian Sea, and south tropical (between 10° and 20°S) and subtropical (between 30° and 40°S) IO, implying less eddy activity in these region. Significant variance anisotropy are seen in the regions of the energetic currents with orientations of the variance ellipses following the directions of mean currents, and they are significantly reduced after excluding the mean, annual, and semiannual components one by one. Generally, both the climatologic MKE and EKE estimated in the present study are qualitatively in agreement with, but quantitatively larger than, estimates from previous studies. Given the most extensive drifter dataset ever assembled to date, as well as the GM decomposition method used that takes into account both the velocity shear and seasonal sampling bias, the estimate of EKE in the present study is believed to be a more accurate estimate and thus is preferable for validating satellite and numerical results.

The near-surface currents in the IO vary significantly at seasonal time scales. In particular, strong annual variability is found in the SC and NMC/SMC regions associated with the annual reversing monsoon, whereas an obvious semiannual cycle is found in the EJs region corresponding to the semiannual westerly component during both intermonsoon seasons. The annual and semiannual variability is found to have significant impacts on the estimate of EKE in the IO, implying that

such low-frequency variability should be carefully taken into account in the estimate of the Lagrangian statistics. This issue is explored in the companion paper PQL2.

REFERENCES

Andersson, M., K. A. Orvik, J. H. LaCasce, I. Koszalka, and C. Mauritzen, 2011: Variability of the Norwegian Atlantic Current and associated eddy field from surface drifters. *J. Geophys. Res.,* **116,** C08032, doi:10.1029/2011JC007078.

Annamalai, H., P. Liu, and S. P. Xie, 2005: Southwest Indian Ocean SST variability: Its local effect and remote influence on Asian monsoons. *J. Climate,* **18,** 4150–4167, doi:10.1175/JCLI3533.1.

Ashok, K., Z. Guan, N. H. Saji, and T. Yamagata, 2004: Individual and combined influences of ENSO and the Indian Ocean dipole on the Indian summer monsoon. *J. Climate,* **17,** 3141–3155, doi:10.1175/1520-0442(2004)017<3141:IACIOE>2.0.CO;2.

Banyte, D., M. Visbeck, T. Tanhua, T. Fischer, G. Krahmann, and J. Karstensen, 2013: Lateral diffusivity from tracer release experiments in the tropical North Atlantic thermocline. *J. Geophys. Res. Oceans,* **118,** 2719–2733, doi:10.1002/jgrc.20211.

Bauer, S., M. S. Swenson, and A. Griffa, 2002: Eddy-mean flow decomposition and eddy-diffusivity estimates in the tropical Pacific Ocean: 2. Results. *J. Geophys. Res.,* **107,** 3154, doi:10.1029/2000JC000613.

Beal, L. M., V. Hormann, R. Lumpkin, and G. R. Foltz, 2013: The response of the surface circulation of the Arabian Sea to monsoonal forcing. *J. Phys. Oceanogr.,* **43,** 2008–2022, doi:10.1175/JPO-D-13-033.1.

Bograd, S. J., R. E. Thomson, A. B. Rabinovich, and P. H. LeBlond, 1999: Near-surface circulation of the northeast Pacific Ocean derived from WOCE-SVP satellite-tracked drifters. *Deep-Sea Res. II,* **46,** 2371–2403, doi:10.1016/S0967-0645(99)00068-5.

Bracco, A., J. H. LaCasce, and A. Provenzale, 2000: Velocity probability density functions for oceanic floats. *J. Phys. Oceanogr.,* **30,** 461–474, doi:10.1175/1520-0485(2000)030<0461:VPDFFO>2.0.CO;2.

Brink, K. H., R. C. Beardsley, P. P. Niiler, M. Abbott, A. Huyer, S. Ramp, T. Stanton, and D. Stuart, 1991: Statistical properties of near-surface flow in the California coastal transition zone. *J. Geophys. Res.,* **96,** 14 693–14 706, doi:10.1029/91JC01072.

Centurioni, L. R., P. P. Niiler, and D.-K. Lee, 2004: Observations of inflow of Philippine sea surface water into the South China Sea through the Luzon Strait. *J. Phys. Oceanogr.,* **34,** 113–121, doi:10.1175/1520-0485(2004)034<0113:OOIOPS>2.0.CO;2.

——, P. N. Niiler, and D.-K. Lee, 2009: Near-surface circulation in the South China Sea during the winter monsoon. *Geophys. Res. Lett.,* **36,** L06605, doi:10.1029/2008GL037076.

Chaigneau, A., and O. Pizarro, 2005: Mean surface circulation and mesoscale turbulent flow characteristics in the eastern South Pacific from satellite tracked drifters. *J. Geophys. Res.,* **110,** C05014, doi:10.1029/2004JC002628.

Chiswell, S. M., 2013: Lagrangian timescales and eddy diffusivity at 1000 m compared to the surface in the South Pacific and Indian Oceans. *J. Phys. Oceanogr.,* **43,** 2718–2732, doi:10.1175/JPO-D-13-044.1.

——, G. J. Rickard, and M. M. Bowen, 2007: Eulerian and Lagrangian eddy statistics of the Tasman Sea and southwest Pacific Ocean. *J. Geophys. Res.,* **112,** C10004, doi:10.1029/2007JC004110.

Cutler, A. N., and J. C. Swallow, 1984: Surface currents of the Indian Ocean (to 25°S, 100°E): Compiled from historical data archived by the Meteorological Office, Bracknell, UK. Institute of Oceanographic Sciences Rep. 187, 8 pp. [Available online at http://eprints.soton.ac.uk/14603/1/14603-01.pdf.]

De Dominicis, M., G. Leuzzi, P. Monti, N. Pinardi, and P.-M. Poulain, 2012: Eddy diffusivity derived from drifter data for dispersion model applications. *Ocean Dyn.,* **62,** 1381–1398, doi:10.1007/s10236-012-0564-2.

Defant, A., 1961: Water bodies and stationary current conditions at boundary surfaces. *Physical Oceanography,* Vol. 1, Pergamon Press, 451–475.

de Ruijter, W. P. M., H. Ridderinkhof, J. R. E. Lutjeharms, M. Schouten, and C. Veth, 2002: Observations of flow in the Mozambique Channel. *Geophys. Res. Lett.,* **29,** doi:10.1029/2001GL013714.

——, H. M. van Aken, E. J. Beier, J. R. E. Lutjeharms, R. P. Matano, and M. W. Schouten, 2004: Eddies and dipoles around south Madagascar: Formation, pathways and large-scale impact. *Deep-Sea Res. I,* **51,** 383–400, doi:10.1016/j.dsr.2003.10.011.

de Verdiere, A. C., 1983: Lagrangian eddy statistics from surface drifters in the eastern North Atlantic. *J. Mar. Res.,* **41,** 375–398, doi:10.1357/002224083788519713.

Du, Y., L. Yang, and S. P. Xie, 2011: Tropical Indian Ocean influence on northwest Pacific tropical cyclones in summer following strong El Niño. *J. Climate,* **24,** 315–322, doi:10.1175/2010JCLI3890.1.

Falco, P., A. Griffa, P.-M. Poulain, and E. Zambianchi, 2000: Transport properties in the Adriatic Sea as deduced from drifter data. *J. Phys. Oceanogr.,* **30,** 2055–2071, doi:10.1175/1520-0485(2000)030<2055:TPITAS>2.0.CO;2.

Figueroa, H. A., and D. B. Olson, 1989: Lagrangian statistics in the South Atlantic as derived from SOS and FGGE drifters. *J. Mar. Res.,* **47,** 525–546, doi:10.1357/002224089785076217.

Hansen, D. V., and P.-M. Poulain, 1996: Quality control and interpolations of WOCE–TOGA drifter data. *J. Atmos. Oceanic Technol.,* **13,** 900–909, doi:10.1175/1520-0426(1996)013<0900:QCAIOW>2.0.CO;2.

Krauss, W., and C. W. Böning, 1987: Lagrangian properties of eddy fields in the northern North Atlantic as deduced from satellite-tracked buoys. *J. Mar. Res.,* **45,** 259–291, doi:10.1357/002224087788401142.

Kug, J.-S., and Y.-G. Ham, 2012: Indian Ocean feedback to the ENSO transition in a multimodel ensemble. *J. Climate,* **25,** 6942–6957, doi:10.1175/JCLI-D-12-00078.1.

Lumpkin, R., 2003: Decomposition of surface drifter observations in the Atlantic Ocean. *Geophys. Res. Lett.,* **30,** 1753, doi:10.1029/2003GL017519.

——, and P. Flament, 2001: Lagrangian statistics in the central North Pacific. *J. Mar. Syst.,* **29,** 141–155, doi:10.1016/S0924-7963(01)00014-8.

——, and M. Pazos, 2007: Measuring surface currents with surface velocity program drifters: The instrument, its data, and some recent results. *Lagrangian Analysis and Predication of Coastal and Ocean Dynamics,* A. Griffa et al., Eds., Cambridge University Press, 39–67.

——, and G. C. Johnson, 2013: Global ocean surface velocities from drifters: Mean, variance, ENSO response, and seasonal cycle. *J. Geophys. Res. Oceans,* **118,** 2992–3006, doi:10.1002/jgrc.20210.

——, A.-M. Treguier, and K. Speer, 2002: Lagrangian eddy scales in the northern Atlantic Ocean. *J. Phys. Oceanogr.,* **32,** 2425–2440, doi:10.1175/1520-0485-32.9.2425.

——, S. A. Grodsky, L. R. Centurioni, M.-H. Rio, J. A. Carton, and D.-K. Lee, 2013: Removing spurious low-frequency variability in drifter velocities. *J. Atmos. Oceanic Technol.,* **30,** 353–360, doi:10.1175/JTECH-D-12-00139.1.

Luo, J.-J., R. Zhang, S. K. Behera, Y. Masumoto, F.-F. Jin, R. Lukas, and T. Yamagata, 2010: Interaction between El Niño and extreme Indian Ocean dipole. *J. Climate,* **23,** 726–742, doi:10.1175/2009JCLI3104.1.

Maurizi, A., A. Griffa, P.-M. Poulain, and F. Tampieri, 2004: Lagrangian turbulence in the Adriatic Sea as computed from drifter data: Effects of inhomogeneity and nonstationarity. *J. Geophys. Res.,* **109,** C04010, doi:10.1029/2003JC002119.

Maximenko, N. A., P. Niiler, L. Centurioni, M.-H. Rio, O. Melnichenko, D. Chambers, V. Zlotnicki, and B. Galperin, 2009: Mean dynamic topography of the ocean derived from satellite and drifting buoy data using three different techniques. *J. Atmos. Oceanic Technol.,* **26,** 1910–1919, doi:10.1175/2009JTECHO672.1.

McCreary, J. P., P. K. Kundu, and R. L. Molinari, 1993: A numerical investigation of dynamics, thermodynamics and mixed-layer processes in the Indian Ocean. *Prog. Oceanogr.,* **31,** 181–244, doi:10.1016/0079-6611(93)90002-U.

Molinari, R. L., D. B. Olson, and G. Reverdin, 1990: Surface current distributions in the tropical Indian Ocean derived from compilations of surface buoy trajectories. *J. Geophys. Res.,* **95,** 7217–7238, doi:10.1029/JC095iC05p07217.

Niiler, P. P., and J. D. Paduan, 1995: Wind-driven motions in the northeast Pacific as measured by Lagrangian drifters. *J. Phys. Oceanogr.,* **25,** 2819–2830, doi:10.1175/1520-0485(1995)025<2819:WDMITN>2.0.CO;2.

Oh, I. S., V. Zhurbas, and W. Park, 2000: Estimating horizontal diffusivity in the East Sea (Sea of Japan) and the northwest Pacific from satellite-tracked drifter data. *J. Geophys. Res.,* **105,** 6483–6492, doi:10.1029/2000JC900002.

Patterson, S. L., 1985: Surface circulation and kinetic energy distributions in the Southern Hemisphere oceans from FGGE drifting buoys. *J. Phys. Oceanogr.,* **15,** 865–884, doi:10.1175/1520-0485(1985)015<0865:SCAKED>2.0.CO;2.

Pazan, S., and P. P. Niiler, 2001: Recovery of near-surface velocity from undrogued drifters. *J. Atmos. Oceanic Technol.,* **18,** 476–489, doi:10.1175/1520-0426(2001)018<0476:RONSVF>2.0.CO;2.

Peng, S., Y.-K. Qian, R. Lumpkin, P. Li, D. Wang, and Y. Du, 2015: Characteristics of the near-surface currents in the Indian Ocean as deduced from satellite-tracked surface drifters. Part II: Lagrangian statistics. *J. Phys. Oceanogr.,* **45,** 459–477, doi:10.1175/JPO-D-14-0049.1.

Perez, R. C., V. Hormann, R. Lumpkin, P. Brandt, W. E. Johns, F. Hernandez, C. Schmid, and B. Bourlès, 2014: Mean meridional currents in the central and eastern equatorial Atlantic. *Climate Dyn.,* **43,** 2943–2962, doi:10.1007/s00382-013-1968-5.

Poulain, P.-M., 2001: Adriatic sea surface circulation as derived from drifter data between 1990 and 1999. *J. Mar. Syst.,* **29,** 3–32, doi:10.1016/S0924-7963(01)00007-0.

——, and P. P. Niiler, 1989: Statistical analysis of the surface circulation in the California Current System using satellite-tracked drifters. *J. Phys. Oceanogr.,* **19,** 1588–1603, doi:10.1175/1520-0485(1989)019<1588:SAOTSC>2.0.CO;2.

——, A. Warn-Varnas, and P. P. Niiler, 1996: Near-surface circulation of the Nordic Seas as measured by Lagrangian drifters. *J. Geophys. Res.,* **101,** 18 237–18 258, doi:10.1029/96JC00506.

——, R. Barbanti, S. Motyzhev, and A. Zatsepin, 2005: Statistical description of the Black Sea near-surface circulation using drifters in 1999–2003. *Deep-Sea Res. I,* **52,** 2250–2274, doi:10.1016/j.dsr.2005.08.007.

Qian, Y.-K., S. Peng, and Y. Li, 2013: Eulerian and Lagrangian statistics in the South China Sea as deduced from surface drifters. *J. Phys. Oceanogr.,* **43,** 726–743, doi:10.1175/JPO-D-12-0170.1.

——, ——, C.-X. Liang, and R. Lumpkin, 2014: On the estimation of Lagrangian diffusivity: Influence of nonstationary mean flow. *J. Phys. Oceanogr.,* **44,** 2796–2811, doi:10.1175/JPO-D-14-0058.1.

Reverdin, G., M. Fieux, J. Gonella, and J. Luyten, 1983: Free drifting buoy measurements in the Indian Ocean equatorial jet. *Hydrodynamics Equatorial Ocean,* J. C. H. Nihoul, Ed., Elsevier, 99–120.

Rinaldi, E., B. B. Nardelli, E. Zambianchi, R. Santoleri, and P.-M. Poulain, 2010: Lagrangian and Eulerian observations of the surface circulation in the Tyrrhenian Sea. *J. Geophys. Res.,* **115,** C04024, doi:10.1029/2009JC005535.

Rupolo, V., B. L. Hua, A. Provenzale, and V. Artale, 1996: Lagrangian velocity spectra at 700 m in the western North Atlantic. *J. Phys. Oceanogr.,* **26,** 1591–1607, doi:10.1175/1520-0485(1996)026<1591:LVSAMI>2.0.CO;2.

Rypina, I. I., I. Kamenkovich, P. Berloff, and L. J. Pratt, 2012: Eddy-induced particle dispersion in the near-surface North Atlantic. *J. Phys. Oceanogr.,* **42,** 2206–2228, doi:10.1175/JPO-D-11-0191.1.

Salas, J., E. García-Ladona, and J. Font, 2001: Statistical analysis of the surface circulation in the Algerian Current using Lagrangian buoys. *J. Mar. Syst.,* **29,** 69–85, doi:10.1016/S0924-7963(01)00010-0.

Sallée, J. B., K. Speer, R. Morrow, and R. Lumpkin, 2008: An estimate of Lagrangian eddy statistics and diffusion in the mixed layer of the Southern Ocean. *J. Mar. Res.,* **66,** 441–463, doi:10.1357/002224008787157458.

Schott, A. F., and J. P. McCreary Jr., 2001: The monsoon circulation of the Indian Ocean. *Prog. Oceanogr.,* **51,** 1–123, doi:10.1016/S0079-6611(01)00083-0.

——, S.-P. Xie, and J. P. McCreary Jr., 2009: Indian Ocean circulation and climate variability. *Rev. Geophys.,* **47,** RG1002, doi:10.1029/2007RG000245.

Schouten, M. W., W. P. M. de Ruijter, and P. J. van Leeuwen, 2002: Upstream control of the Agulhas ring shedding. *J. Geophys. Res.,* **107,** 3109, doi:10.1029/2001JC000804.

——, ——, ——, and R. Ridderinkhof, 2003: Eddies and variability in the Mozambique Channel. *Deep-Sea Res. II,* **50,** 1987–2003, doi:10.1016/S0967-0645(03)00042-0.

Shenoi, S. S. C., P. K. Saji, and A. M. Almeida, 1999: Near-surface circulation and kinetic energy in the tropical Indian Ocean derived from Lagrangian drifters. *J. Mar. Res.,* **57,** 885–907, doi:10.1357/002224099321514088.

Shetye, S. R., and G. S. Michael, 1988: Satellite-tracked drifting buoy observations in the south equatorial current in the Indian Ocean. *Proc. Indian Acad. Sci.,* **97,** 149–157, doi:10.1007/BF02861850.

——, and A. D. Gouveia, 1998: Coastal circulation in the north Indian Ocean: Coastal segment (14,S-W). *The Global Coastal Ocean: Regional Studies and Syntheses,* A. R. Robinson and K. H. Brink, Eds., John Wiley and Sons, 523–556.

Sudre, J., and R. A. Morrow, 2008: Global surface currents: A high-resolution product for investigating ocean dynamics. *Ocean Dyn.,* **58,** 101–118, doi:10.1007/s10236-008-0134-9.

——, C. Maes, and G. Véronique, 2013: On the global estimates of geostrophic and Ekman surface currents. *Limnol. Oceanogr. Fluids Environ.,* **3,** 1–20, doi:10.1215/21573689-2071927.

Swart, N. C., J. R. E. Lutjeharms, H. Ridderinkhof, and W. P. M. de Ruijter, 2010: Observed characteristics of Mozambique Channel eddies. *J. Geophys. Res.,* **115,** C09006, doi:10.1029/2009JC005875.

Swenson, M. S., and P. P. Niiler, 1996: Statistical analysis of the surface circulation of the California Current. *J. Geophys. Res.,* **101,** 22 631–22 645, doi:10.1029/96JC02008.

Ursella, L., P.-M. Poulain, and R. P. Signell, 2007: Surface drifter derived circulation in the northern and middle Adriatic Sea: Response to wind regime and season. *J. Geophys. Res.,* **112,** C03S04, doi:10.1029/2005JC003177.

Veneziani, M., A. Griffa, A. M. Reynolds, and A. J. Mariano, 2004: Oceanic turbulence and stochastic models from subsurface Lagrangian data for the northwest Atlantic Ocean. *J. Phys. Oceanogr.,* **34,** 1884–1906, doi:10.1175/1520-0485(2004)034<1884:OTASMF>2.0.CO;2.

Woodberry, K. E., M. E. Luther, and J. J. O'Brien, 1989: The wind-driven seasonal circulation in the southern tropical Indian Ocean. *J. Geophys. Res.,* **94,** 17 985–18 002, doi:10.1029/JC094iC12p17985.

Wu, R., and B. P. Kirtman, 2007: Role of the Indian Ocean in the biennial transition of the Indian summer monsoon. *J. Climate,* **20,** 2147–2164, doi:10.1175/JCLI4127.1.

Wunsch, C., 1996: *The Ocean Circulation Inverse Problem.* Cambridge University, 442 pp.

Wyrtki, K., L. Magaard, and J. Hager, 1976: Eddy energy in the oceans. *J. Geophys. Res.,* **81,** 2641–2646, doi:10.1029/JC081i015p02641.

Xie, S. P., K. Hu, J. Hafner, H. Tokinaga, Y. Du, G. Huang, and T. Sampe, 2009: Indian Ocean capacitor effect on Indo–western Pacific climate during the summer following El Niño. *J. Climate,* **22,** 730–747, doi:10.1175/2008JCLI2544.1.

Yang, J., Q. Liu, and Z. Liu, 2010: Linking observations of the Asian monsoon to the Indian Ocean SST: Possible roles of Indian Ocean basin mode and dipole mode. *J. Climate,* **23,** 5889–5902, doi:10.1175/2010JCLI2962.1.

Zhang, H.-M., M. D. Prater, and T. Rossby, 2001: Isopycnal La-grangian statistics from the North Atlantic current RAFOS float observations. *J. Geophys. Res.,* **106,** 13 817–13 836, doi:10.1029/1999JC000101.

Zheng, S.-J., Y.-H. Zhang, W. Zhuang, J.-X. Li, and Y. Du, 2012: Typical surface seasonal circulation in the Indian Ocean derived from Argos floats. *Atmos. Oceanic Sci. Lett.,* **5,** 329–333.

Zheng, X.-T., S. P. Xie, and Q. Liu, 2011: Response of the Indian Ocean basin mode and its capacitor effect to global warming. *J. Climate,* **24,** 6146–6164, doi:10.1175/2011JCLI4169.1.

Zhurbas, V., and I. S. Oh, 2003: Lateral diffusivity and Lagrangian scales in the Pacific Ocean as derived from drifter data. *J. Geophys. Res.,* **108,** 3141, doi:10.1029/2002JC001596.

——, and ——, 2004: Drifter-derived maps of lateral diffusivity in the Pacific and Atlantic Oceans in relation to surface circu-lation patterns. *J. Geophys. Res.,* **109,** C05015, doi:10.1029/2003JC002241.

——, D. Lyzhkov, and N. Kuzmina, 2014: Drifter-derived estimates of lateral eddy diffusivity in the world ocean with emphasis on the Indian Ocean and problems of parameterization. *Deep-Sea Res. I,* **83,** 1–11, doi:10.1016/j.dsr.2013.09.001.